Saturation of water reflectance in extremely turbid media based on field measurements, satellite data and bio-optical modelling

Yafei Luo, David Doxaran, Kevin Ruddick, Fang Shen, Bernard Gentili, Liwen Yan, Haijun Huang

▶ To cite this version:

HAL Id: hal-02352140
https://hal.archives-ouvertes.fr/hal-02352140

Submitted on 6 Nov 2019

Saturation of water reflectance in extremely turbid media based on field measurements, satellite data and bio-optical modelling

YAFEI LUO,[1,2,3] DAVID DOXARAN,[3,7] KEVIN RUDDICK,[4] FANG SHEN,[5] BERNARD GENTILI,[6] LIWEN YAN,[1] AND HAIJUN HUANG[1,2,8]

[1]*Institute of Oceanology, Chinese Academy of Sciences, Qingdao 266071, China*
[2]*University of Chinese Academy of Sciences, Beijing 100049, China*
[3]*Sorbonne Université, CNRS, Laboratoire d'Océanographie de Villefanche, LOV, Villefranche-sur-mer 06230, France*
[4]*Royal Belgian Institute for Natural Sciences, Operational Directorate Natural Environments, Brussels 1200, Belgium*
[5]*State Key Laboratory of Estuarine and Coastal Research, East China Normal University, Shanghai 200062, China*
[6]*6 avenue Lympia, 06300 Nice, France*
[7]*doxaran@obs-vlfr.fr*
[8]*hjhuang@qdio.ac.cn*

Abstract: Evidence of water reflectance saturation in extremely turbid media is highlighted based on both field measurements and satellite data corrected for atmospheric effects. This saturation is obvious in visible spectral bands, i.e., in the blue, green and even red spectral regions when the concentration of suspended particulate matter (SPM) reaches then exceeds 100 to 1000 g.m^{-3}. The validity of several bio-optical semi-analytical models is assessed in the case of highly turbid waters, based on comparisons with outputs of the Hydrolight radiative transfer model. The most suitable models allow to reproduce the observed saturation and, by inversion, to retrieve information on the SPM mass-specific inherent optical properties.

References and links

1. D. Doxaran, J.-M. Froidefond, S. Lavender, and P. Castaing, "Spectral signature of highly turbid waters: Application with SPOT data to quantify suspended particulate matter concentrations," Remote Sens. Environ. **81**(1), 149–161 (2002).
2. B. Nechad, K. Ruddick, and Y. Park, "Calibration and validation of a generic multisensor algorithm for mapping of total suspended matter in turbid waters," Remote Sens. Environ. **114**(4), 854–866 (2010).
3. C. D. Mobley, *Light and Water: Radiative Transfer in Natural Waters* (Academic, 1994).
4. R. Doerffer and H. Schiller, "The MERIS Case 2 water algorithm," Int. J. Remote Sens. **28**(3–4), 517–535 (2007).
5. H. R. Gordon, O. B. Brown, R. H. Evans, J. W. Brown, R. C. Smith, K. S. Baker, and D. K. Clark, "A semianalytic radiance model of ocean color," J. Geophys. Res. **93**(D9), 10909–10924 (1988).
6. Z. Lee, K. L. Carder, and K. Du, "Effects of molecular and particle scatterings on the model parameter for remote-sensing reflectance," Appl. Opt. **43**(25), 4957–4964 (2004).
7. Z. Lee, S. Shang, G. Lin, J. Chen, and D. Doxaran, "On the modeling of hyperspectral remote-sensing reflectance of high-sediment-load waters in the visible to shortwave-infrared domain," Appl. Opt. **55**(7), 1738–1750 (2016).
8. P. Kubelka and F. Munk, "Ein beitrag zur optik der farbanstriche," Zeritschrift fr. Tech. Phys. **12**, 593–601 (1931).
9. F. Shen, W. Verhoef, Y. Zhou, M. S. Salama, and X. Liu, "Satellite estimates of wide-range suspended sediment concentrations in Changjiang (Yangtze) estuary using MERIS data," Estuaries Coasts **33**(6), 1420–1429 (2010).
10. F. Shen, Y. Zhou, J. Li, Q. He, and W. Verhoef, "Remotely sensed variability of the suspended sediment concentration and its response to decreased river discharge in the Yangtze estuary and adjacent coast," Cont. Shelf Res. **69**, 52–61 (2013).

11. M. S. Salama and W. Verhoef, "Two-stream remote sensing model for water quality mapping: 2SeaColor," Remote Sens. Environ. **157**, 111–122 (2015).

12. E. Knaeps, K. Ruddick, D. Doxaran, A. Dogliotti, B. Nechad, D. Raymaekers, and S. Sterckx, "A SWIR based algorithm to retrieve total suspended matter in extremely turbid waters," Remote Sens. Environ. **168**, 66–79 (2015).

13. S. Novoa, D. Doxaran, A. Ody, Q. Vanhellemont, V. Lafon, B. Lubac, and P. Gernez, "Atmospheric Corrections and Multi-Conditional Algorithm for Multi-Sensor Remote Sensing of Suspended Particulate Matter in Low-to-High Turbidity Levels Coastal Waters," Remote Sens. **9**(1), 61 (2017).

14. W. Shi and M. Wang, "Ocean reflectance spectra at the red, near-infrared, and shortwave infrared from highly turbid waters: A study in the Bohai Sea, Yellow Sea, and East China Sea," Limnol. Oceanogr. **59**(2), 427–444 (2014).

15. K. G. Ruddick, V. De Cauwer, Y. J. Park, and G. Moore, "Seaborne measurements of near infrared water-leaving reflectance: The similarity spectrum for turbid waters," Limnol. Oceanogr. **51**(2), 1167–1179 (2006).

16. T. Leeuw and E. Boss, "The HydroColor App: Above Water Measurements of Remote Sensing Reflectance and Turbidity Using a Smartphone Camera," Sensors (Basel) **18**(1), 256 (2018).

17. D. Doxaran, J.-M. Froidefond, P. Castaing, and M. Babin, "Dynamics of the turbidity maximum zone in a macrotidal estuary (the Gironde, France): Observations from field and MODIS satellite data," Estuar. Coast. Shelf Sci. **81**(3), 321–332 (2009).

18. Q. Vanhellemont and K. Ruddick, "Advantages of high quality SWIR bands for ocean colour processing: Examples from Landsat-8," Remote Sens. Environ. **161**, 89–106 (2015).

19. Q. Vanhellemont and K. Ruddick, "Turbid wakes associated with offshore wind turbines observed with Landsat 8," Remote Sens. Environ. **145**, 105–115 (2014).

20. L. G. Olmanson, P. L. Brezonik, J. C. Finlay, and M. E. Bauer, "Comparison of Landsat 8 and Landsat 7 for regional measurements of CDOM and water clarity in lakes," Remote Sens. Environ. **185**, 119–128 (2016).

21. Z. Qiu, C. Xiao, W. Perrie, D. Sun, S. Wang, H. Shen, D. Yang, and Y. He, "Using Landsat 8 data to estimate suspended particulate matter in the Yellow River estuary," J. Geophys. Res. Oceans **122**(1), 276–290 (2017).

22. C. D. Mobley, "Estimation of the remote-sensing reflectance from above-surface measurements," Appl. Opt. **38**(36), 7442–7455 (1999).

23. R. M. Pope and E. S. Fry, "Absorption spectrum (380-700 nm) of pure water. II. Integrating cavity measurements," Appl. Opt. **36**(33), 8710–8723 (1997).

24. A. Morel and R. C. Smith, "Relation between total quanta and total energy for aquatic photosynthesis," Limnol. Oceanogr. **19**(4), 591–600 (1974).

25. A. Morel, "Optical properties of pure water and pure sea water," Opt. Aspects Oceanography **1**, 1–24 (1974).

26. Z. Lee, J. Wei, K. Voss, M. Lewis, A. Bricaud, and Y. Huot, "Hyperspectral absorption coefficient of "pure" seawater in the range of 350–550 nm inverted from remote sensing reflectance," Appl. Opt. **54**(3), 546–558 (2015).

27. M. Babin, D. Stramski, G. M. Ferrari, H. Claustre, A. Bricaud, G. Obolensky, and N. Hoepffner, "Variations in the light absorption coefficients of phytoplankton, nonalgal particles, and dissolved organic matter in coastal waters around Europe," J. Geophys. Res. **108**(C7), 3211 (2003).

28. D. Doxaran, N. Cherukuru, and S. J. Lavender, "Apparent and inherent optical properties of turbid estuarine waters: measurements, empirical quantification relationships, and modeling," Appl. Opt. **45**(10), 2310–2324 (2006).

29. H. R. Gordon and A. Y. Morel, *Remote Assessment of Ocean Color for Interpretation of Satellite Visible imagery: A Review* (Springer Science & Business Media, 1983), Vol. 4.

30. Z. Lee, K. L. Carder, and R. A. Arnone, "Deriving inherent optical properties from water color: a multiband quasi-analytical algorithm for optically deep waters," Appl. Opt. **41**(27), 5755–5772 (2002).

31. M. Babin, A. Morel, V. Fournier-Sicre, F. Fell, and D. Stramski, "Light scattering properties of marine particles in coastal and open ocean waters as related to the particle mass concentration," Limnol. Oceanogr. **48**(2), 843–859 (2003).

32. D. Stramski, S. B. Woźniak, and P. J. Flatau, "Optical properties of Asian mineral dust suspended in seawater," Limnol. Oceanogr. **49**(3), 749–755 (2004).

33. G. Neukermans, H. Loisel, X. Mériaux, R. Astoreca, and D. McKee, "In situ variability of mass-specific beam attenuation and backscattering of marine particles with respect to particle size, density, and composition," Limnol. Oceanogr. **57**(1), 124–144 (2012).

34. D. Sun, Z. Qiu, C. Hu, S. Wang, L. Wang, L. Zheng, T. Peng, and Y. He, "A hybrid method to estimate suspended particle sizes from satellite measurements over Bohai Sea and Yellow Sea," J. Geophys. Res. Oceans **121**(9), 6742–6761 (2016).

35. R. Astoreca, D. Doxaran, K. Ruddick, V. Rousseau, and C. Lancelot, "Influence of suspended particle concentration, composition and size on the variability of inherent optical properties of the Southern North Sea," Cont. Shelf Res. **35**, 117–128 (2012).

36. M. Babin and D. Stramski, "Variations in the mass-specific absorption coefficient of mineral particles suspended in water," Limnol. Oceanogr. **49**(3), 756–767 (2004).

37. D. Doxaran, M. Babin, and E. Leymarie, "Near-infrared light scattering by particles in coastal waters," Opt. Express **15**(20), 12834–12849 (2007).

38. D. Bowers, G. Harker, and B. Stephan, "Absorption spectra of inorganic particles in the Irish Sea and their relevance to remote sensing of chlorophyll," Int. J. Remote Sens. **17**(12), 2449–2460 (1996).
39. D. Bowers and C. Binding, "The optical properties of mineral suspended particles: A review and synthesis," Estuar. Coast. Shelf Sci. **67**(1), 219–230 (2006).
40. C. L. Gallegos, D. L. Correll, and J. W. Pierce, "Modeling spectral diffuse attenuation, absorption, and scattering coefficients in a turbid estuary," Limnol. Oceanogr. **35**(7), 1486–1502 (1990).
41. Z. Lee, K. L. Carder, C. D. Mobley, R. G. Steward, and J. S. Patch, "Hyperspectral remote sensing for shallow waters. 2. Deriving bottom depths and water properties by optimization," Appl. Opt. **38**(18), 3831–3843 (1999).
42. H. Loisel and A. Morel, "Non-isotropy of the upward radiance field in typical coastal (Case 2) waters," Int. J. Remote Sens. **22**(2–3), 275–295 (2001).
43. W. E. Vargas and G. A. Niklasson, "Applicability conditions of the Kubelka-Munk theory," Appl. Opt. **36**(22), 5580–5586 (1997).
44. C. Sandoval and A. D. Kim, "Deriving Kubelka-Munk theory from radiative transport," J. Opt. Soc. Am. A **31**(3), 628–636 (2014).
45. B. Nechad, K. Ruddick, and G. Neukermans, "Calibration and validation of a generic multisensor algorithm for mapping of turbidity in coastal waters," in *SPIE Europe Remote Sensing*, (International Society for Optics and Photonics, 2009), 74730H.
46. A. Morel and B. Gentili, "Diffuse reflectance of oceanic waters. II Bidirectional aspects," Appl. Opt. **32**(33), 6864–6879 (1993).
47. A. Morel and B. Gentili, "Diffuse reflectance of oceanic waters. III. Implication of bidirectionality for the remote-sensing problem," Appl. Opt. **35**(24), 4850–4862 (1996).
48. E. Boss, W. H. Slade, M. Behrenfeld, and G. Dall'Olmo, "Acceptance angle effects on the beam attenuation in the ocean," Opt. Express **17**(3), 1535–1550 (2009).
49. E. Leymarie, D. Doxaran, and M. Babin, "Uncertainties associated to measurements of inherent optical properties in natural waters," Appl. Opt. **49**(28), 5415–5436 (2010).
50. D. Doxaran, E. Leymarie, B. Nechad, A. Dogliotti, K. Ruddick, P. Gernez, and E. Knaeps, "Improved correction methods for field measurements of particulate light backscattering in turbid waters," Opt. Express **24**(4), 3615–3637 (2016).

1. Introduction

Sediment-dominated turbid waters such as estuaries, bays and river mouths play an important role in coastal zones in terms of exchanges of matter between land and ocean, water quality and primary production. The concentration of suspended particulate matter (SPM) in such waters can be estimated using ocean color satellite data corrected for atmospheric effects using empirical [1], semi-analytical [2] or multispectral empirical fitting (e.g., neural networks) relationships between the water reflectance at the appropriate spectral band and SPM concentration. The water inherent optical properties (IOPs), namely the light backscattering and absorption coefficients, can also be retrieved by inversion of the remote sensing reflectance (R_{rs}) or equivalent water-leaving reflectance (ρ_w) signal. This inversion can be achieved by comparing R_{rs} data with simulated spectra generated by a radiative transfer model (e.g., Hydrolight [3]) using a neural network or similar technique [4]. Alternatively, the relationship between R_{rs} and IOPs can be approximated by a semi-analytical reflectance model such as those developed by Gordon et al. [5], Lee et al. (2004) [6,7] or Kubelka and Munk [8–11] (this latter one being specifically designed for highly scattering media).

In highly turbid waters, several studies based on field and laboratory measurements have shown that the water-leaving reflectance signal tends towards an asymptotic value, termed hereafter "saturation reflectance", for increasing SPM concentration [1,9,12–16]. This saturation occurs first at short visible wavelengths then progressively in the green and even in the red and near-infrared (NIR) spectral regions when the SPM concentration becomes extremely high (~1000 g.m^{-3}). As an example, Fig. 1 shows typical in situ measurements of ρ_w spectra for SPM concentrations increasing from 3 to 1525 g.m^{-3} in the turbid waters of the Gironde Estuary (derived from Fig. 2(a) in Novoa et al. (2017) [13]). The saturation of ρ_w spectra at short visible wavelengths (blue to green spectral regions) is obvious when SPM concentration is higher than 70 g.m^{-3}; ρ_w also starts to saturate in the red spectral region (600–700 nm) for SPM concentration higher than 600 g.m^{-3}. The ρ_w signal is then no longer sensitive to variations of SPM concentration. According notably to Doxaran et al. (2002) [1],

this can be explained using bio-optical models which relate the water reflectance to the ratio between light backscattering and light absorption [5–11]. When SPM is high enough, the contribution of SPM to both light absorption and light backscattering at a specific wavelength becomes predominant (i.e., the contributions of water molecules and colored dissolved organic matter are then negligible). As light backscattering and light absorption by SPM can be written as the products between the SPM concentration and the SPM mass-specific backscattering and absorption coefficients, when the water reflectance becomes saturated it is no longer sensitive to variations of the SPM concentration. It reaches a constant value which mainly depends on the SPM mass-specific backscattering and absorption coefficients. As SPM concentration increases, saturation of water reflectance first occurs at short visible wavelengths where light absorption by water molecules is low (so that the SPM contribution is rapidly predominant), then progressively in the green, red and even NIR spectral regions where light absorption by water molecules is respectively higher [12,14].
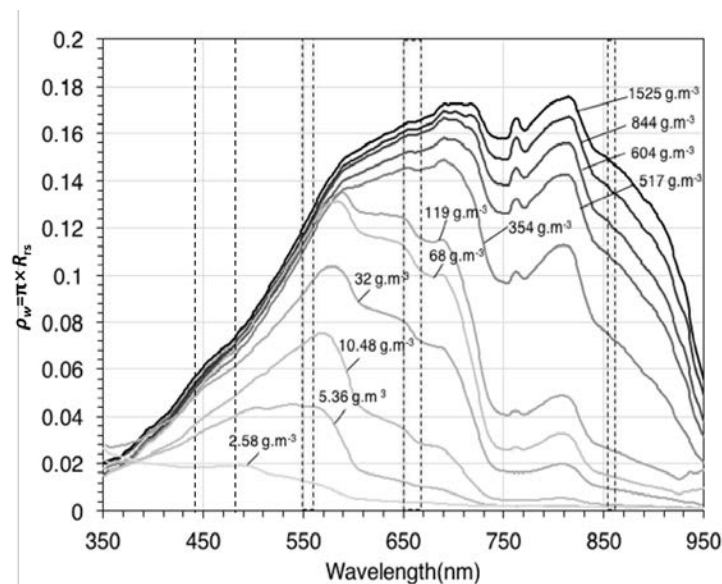

Fig. 1. Selected water-leaving reflectance spectra (ρ_w) for increasing SPM concentration (g.m^{-3}) based on field measurements in the Gironde Estuary. Background figure was reproduced from Novoa et al. (2017) [13]. Dashed lines are the wavebands of the satellite sensor selected in this study.

To our knowledge, the saturation of water reflectance has never been observed/analyzed from satellite data and no one has yet tried to extract from it relevant information on the SPM mass-specific IOPs. The main objective of the present study is precisely to observe the saturation of the water reflectance in extremely turbid waters and then retrieve information on the mass-specific absorption and backscattering coefficients of suspended particles from this saturation of water reflectance by using adapted semi-analytical reflectance models. This saturation is first analyzed based on in situ measurements then on satellite data corrected for atmospheric effects using algorithms designed for highly turbid waters. Three test sites characterized by extremely turbid waters are considered [Fig. 2]: the Gironde Estuary (GRE, South-West of France), the Yellow River Estuary (YRE) and the Subei Shallow Bank (SSB) along the East coast of China. The inversion of saturated water reflectance values into SPM mass-specific IOPs (backscattering to absorption coefficients ratios, $b_{bp}*/a_p*$) is then tested and results are discussed.
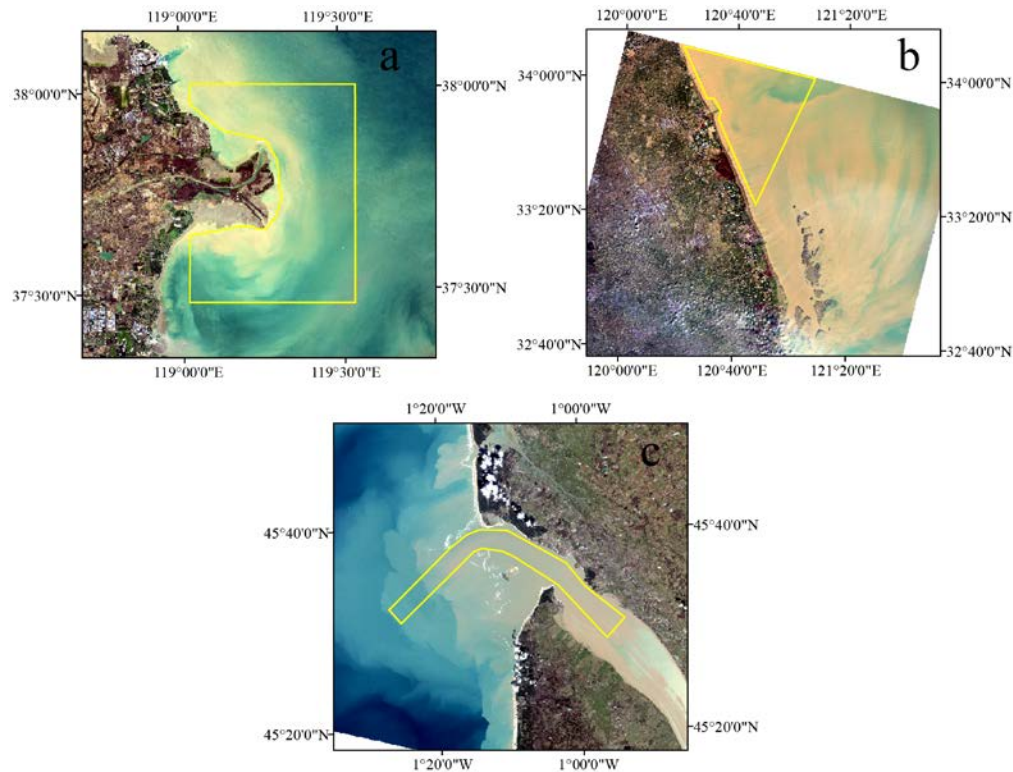
Fig. 2. Maps of the three test sites produced based on L8/OLI satellite data (top of the atmosphere quasi-true color images): (a) the Yellow River Estuary (YRE, 27 October 2015), (b) the Subei Shallow Bank (SSB, 8 March 2017) and (c) the Gironde Estuary (GRE, 22 February 2015). The yellow polygons delimit the areas of interest.

2. Data and methods

2.1 In situ data

In situ radiometric (R_{rs}) and near-surface SPM concentration measurements were carried out in the Gironde Estuary during a field campaign in August 2013 comprising 35 samples. Detailed information on sampling, measurement protocols and data processing can be found in Knaeps et al. (2015) [12]. The Gironde Estuary is a highly turbid macro-tidal estuary [17] located in South-West France [Fig. 2]. SPM concentrations within surface waters ranged from 68 to 1525 g.m^{-3} during this 2013 field campaign. The R_{rs} spectra (350–950 nm) (R_{rs} ranging from 0.01 to 0.056 sr^{-1} at 815 nm) were obtained from independent Trios and ASD above-water measurements of the upwelling radiance, sky radiance and downwelling irradiance. A careful inspection of each measured spectrum revealed that sensor saturation was never reached. Results from the two data sets in terms of R_{rs} values showed a very good agreement [see Fig. 3 in [12]].

In the blue to green visible spectral region (350 nm to 580 nm), R_{rs} was first observed to increase for SPM concentration increasing up to about 60 g.m^{-3} but did not vary much over this concentration. Similarly, in the red spectral region (600-700 nm), R_{rs} was observed first to increase with SPM concentration increasing up to about 500 g.m^{-3}, then also tended to saturate towards an asymptotic limit, in agreement with the model developed by Nechad et al. (2010) [2]. In the NIR (800-900 nm), R_{rs} showed large variations and was clearly sensitive to SPM variations ([12], [Fig. 1]).

2.2 Satellite data

The choice in this study was to use Landsat8 Operational Land Imager (L8/OLI) satellite data. The OLI sensor has high-quality shortwave-infrared (SWIR) spectral bands well designed for the atmospheric correction of data recorded in the visible and NIR wavebands over such turbid waters [13,18]. The specifications of L8/OLI satellite data, in terms of radiometric sensitivity (12-bit resolution), spectral (with respectively four, one and two wavebands in the visible, NIR and SWIR spectral regions) and spatial (30 m) resolutions, are well adapted for the remote sensing of (extremely) high SPM concentrations in the maximum turbidity zones usually encountered in estuaries, bays and river plumes [13,18–21].

We considered a selection of cloud-free L8/OLI images recorded from 2013 to 2017 over the three test sites, e.g., one recorded on 27 October 2015 over the YRE, one on 8 March 2017 over the SSB and one on 22 February 2015 over the GRE [Fig. 2]. The data recorded at the top of the atmosphere (TOA) clearly show highly turbid waters for the well-known maximum turbidity zones of the three estuaries. However, the OLI sensor did not saturate over the most turbid waters observed as (much) higher TOA reflectance values were systematically recorded over surrounding land and/or cloud pixels. All OLI images were processed with the ACOLITE software (version 20170718.0) [18,19], applying the SWIR atmospheric correction algorithm [18], as recommended in the case of highly turbid waters [13], to retrieve ρ_w values in the visible and NIR OLI spectral bands centered at 443, 483, 561, 655 and 865 nm.

2.3 Methods

The general method was in three steps: (i) first observe, from both in situ and satellite data measured for turbid to extremely turbid estuarine waters, the saturation of water reflectance; (ii) then reproduce the observed saturation using a semi-analytical bio-optical model valid in the case of highly turbid waters; (iii) finally derive from the observed and modelled saturated reflectance values relevant information on the SPM mass-specific IOPs.

Before detailing the computations made using different bio-optical models, we provide a theoretical background with definitions of the water reflectance and how it can be modeled as a function of the IOPs and SPM concentration.

2.3.1 Theoretical background

Radiative transfer models (e.g., Hydrolight [3]) reproduce the propagation of directional light (radiance L in $W.sr^{-1}.m^{-2}.nm^{-1}$) within the water column and through the water/air interface, depending on sky conditions, water surface roughness and water IOPs (absorption coefficient and Volume Scattering Function (VSF), the IOP which defines both the backscattering coefficient and the scattering phase function). The main parameter of interest when dealing with ocean color satellite data is the remote-sensing reflectance, R_{rs} in sr^{-1}, defined as the ratio between the water-leaving radiance (L_w) and the downwelling irradiance (E_d, in $W.m^{-2}.nm^{-1}$) just above the water surface [22]:

$$R_{rs}(\theta, \phi, \lambda) = L_w(\theta, \phi, \lambda) / E_d(\lambda). \tag{1}$$

This parameter is directional, i.e., it depends on the viewing geometry of the L_w signal. This geometry is defined by the polar (θ) and azimuthal (ϕ) angles, respectively, while l is the wavelength.

The dimensionless water-leaving reflectance is related to R_{rs} through:

$$\rho_w = \pi \times R_{rs.} \tag{2}$$

2.3.2 Semi-analytical reflectance models

The water reflectance is assumed to be a function of two IOPs, the total absorption and backscattering coefficients, a and b_b in m^{-1}, which are the sums of the contributions of the colored water constituents: water molecules, colored dissolved organic matter (CDOM) and SPM (phytoplankton and non-algal particles). In the case of turbid sediment-dominated waters, the contributions of CDOM and phytoplankton can be neglected so that a and b_b can be written as [1,7]:

$$a = a_w + SPM \times a_p^*,$$
(3)

$$b_b = b_{bw} + SPM \times b_{bp}^*,$$
(4)

Where a_w and b_{bw} are the absorption and backscattering coefficients of pure water and are known values [23–26]; SPM (in g.m^{-3}) is the SPM concentration (mainly non-algal particles); a^*_p and b^*_{bp} (in m^2.g^{-1}) are the SPM mass-specific absorption and backscattering coefficients and their spectral variations are often modelled as [7,27–31]:

$$a_p^*(\lambda) = a_p^*(443) \times \exp(-s \times (\lambda - 443)),$$
(5)

$$b_{bp}^*(\lambda) = b_{bp}^*(555) \times (\lambda / 555)^{-\gamma},$$
(6)

Where s (nm^{-1}) is the spectral slope of the mass-specific absorption coefficient and g is the spectral exponent of the mass-specific backscattering coefficient. Based on field measurements reported in the literature [27–40], the ranges of $a^*p(443)$, s, $b^*bp(555)$ and g values in coastal waters are reported in Table 1.

The absorption and backscattering coefficients of water for increasing turbidity (SPM concentration increasing from 10 to 2000 g.m^{-3}) were modelled according to Eqs. (3)-(6).

Table 1. Inputs in Hydrolight simulations.

Parameter	Value
Wavelength (nm)	443, 483, 561, 655, 865
SPM (g.m^{-3})	10, 20, 50, 100, 200, 500, 1000, 2000
$a^*p(443)$ (m^2.g^{-1})	0.025, 0.05
$b^*p(555)$ (m^2.g^{-1})	0.2, 0.5, 1
s (nm^{-1})	0.005, 0.012, 0.02
g	0, 0.5, 1
SPM scattering phase function	FFbb030

Using Hydrolight, the subsurface and above-water remote sensing reflectance signals (respectively noted r_{rs} and R_{rs}, in sr^{-1}) were computed at the nadir viewing direction at 443, 483, 561, 665 and 865 nm (central wavelengths of OLI spectral bands), for a Sun at zenith with no cloud and no wind, selecting the navy aerosol model, 80% of humidity and for a visibility of 19.5 km. The IOPs described in Table 1 were considered as inputs. The ratio between the upwelling irradiance and upwelling radiance, Q in sr, was also computed in the nadir direction. The phase function for particle scattering was based on Fournier and Forand with a backscattering to scattering ratio of 3% [7], noted FFbb030.

Hydrolight outputs were then used as a reference to assess the respective performance of three different semi-analytical bio-optical models. The first one is the Gordon model (GM) [5] which relates r_{rs} to the IOPs based on a second-order polynomial relationship established from Monte-Carlo calculations:

$$r_{rs} = \sum_{i=1}^{2} l_i \left(\frac{b_b}{a + b_b}\right)^i$$
(7)

Where the l_i coefficients depend on illumination conditions and on the SPM scattering phase function. We considered three different sets of l_i coefficients [5,41,42]: $(l_1, l_2) = (0.0949, 0.0794)$ (GM_1), $(l_1, l_2) = (0.084, 0.170)$ (GM_2) and $(l_1, l_2) = (0.13, 0.0)$ (GM_3).

The second model is the Lee et al. (2004) model (LM) [6,7]. It is a modified version of the Gordon model in which the l_i coefficients (Eq. (7)) are no longer constant values but are related to the IOPs through a function (G):

$$G = G_0 \frac{b_{bw}}{b_{bw} + b_{bp}} + G_1 \left(1 - G_2 \exp\left(-G_3 \frac{b_{bp}}{a + b_b}\right)\right) \frac{b_{bp}}{b_{bw} + b_{bp}}, \qquad (8a)$$

$$r_{rs} = G \frac{b_b}{a + b_b} \qquad (8b)$$

Where G_0, G_1, G_2 and G_3 are constant values (0.113, 0.197, 0.636 and 2.552, respectively) obtained by fitting Eq. (8a) to outputs from Hydrolight computations for a viewing angle at nadir and an average particle phase function [6].

The third model is the Kubelka and Munk model (KM) [8–11]. It is designed for highly scattering media [43,44] and may thus be useful for highly turbid waters. It relates R, the irradiance reflectance just below the water surface (i.e., the ratio between the upwelling and downwelling irradiance signals at null depth), then r_{rs}, to the backscattering to absorption ratio according to:

$$R = \frac{b_b}{b_b + a + \sqrt{a(2b_b + a)}} = \frac{b_b / a}{1 + b_b / a + \sqrt{1 + 2b_b / a}}, \qquad (9a)$$

$$r_{rs} = R / Q. \qquad (9b)$$

Here we considered two different versions of the Kubelka and Munk model: one using the exact Q values computed using Hydrolight (KM_HQ) and a second one with a constant Q value of 3.6 sr (KM_CQ), i.e., the mean value obtained from our Hydrolight computations.

Using the exact same inputs as in Hydrolight simulations [Table 1], r_{rs} was computed using Gordon models (GM_1, GM_2, GM_3), Lee et al. (2004) model (LM) and Kubelka and Munk models (KM_HQ, KM_CQ). Hydrolight results were then used as reference in order to determine which of these semi-analytical models reproduce well the saturation of water reflectance in highly turbid waters and could be used further to retrieve information of SPM mass-specific IOPs.

2.3.3 Saturation criterion

As R_{rs} in the NIR does not saturate until extreme SPM concentrations of about 2000 g.m^{-3} [12,13], a simple way to observe the saturation of R_{rs} in OLI visible spectral bands for increasing SPM concentration is to plot R_{rs} as a function of $R_{rs}(865)$. To model the progressive saturation of R_{rs} in visible spectral bands, four types of relationships were considered to fit the in situ and satellite data: logarithmic, polynomial (quadratic), power-law and Nechad-type (Eq. (10)) [2]. The best-fitted curves were systematically obtained using the Nechad-type relationship. Moreover, this function is asymptotic, thus adapted to reproduce the R_{rs} saturation. The Nechad-type relationship was consequently selected to fit the in situ and satellite data, i.e., to model the progressive saturation of R_{rs} in visible spectral bands and determine an objective criterion for saturation. It is written as [2]:

$$R_{rs} = \frac{X}{A_\rho + X / C_\rho} \qquad (10)$$

With A_ρ and C_ρ two calibration coefficients. A_ρ is proportional to the ratio between the absorption coefficient of non-particle optically-active substances (essentially pure water molecules and colored dissolved organic matter) and the SPM mass-specific backscattering coefficient. C_ρ is a function of the ratio between the SPM mass-specific backscattering and absorption coefficients. X is here either the SPM concentration or $R_{rs}(865)$. A_ρ and C_ρ can be computed from field or satellite data using the non-linear least square method. C_ρ gives the saturation asymptote [2,45]. R_{rs} (at 443, 483, 561 or 655 nm) saturates when it reaches the saturation value of C_ρ.

3. Results and discussion

3.1 Observations of reflectance saturation in extremely turbid waters

Based on field measurements in the GRE, the rapid saturation of R_{rs} for SPM concentrations higher than 100 g.m^{-3} is clearly observed at short visible wavelengths (here 443 and 483 nm) [Fig. 3(a)]. Saturation is also observed at 561 nm when the SPM concentration gets higher than 150 g.m^{-3}. At 655 nm, R_{rs} is almost saturated when the SPM concentration is higher than 500 g.m^{-3}, while saturation of the R_{rs} signal at 865 nm only starts occurring for extremely high SPM concentrations (> 1000 g.m^{-3}). It is also possible to examine the progressive saturation of R_{rs} at OLI visible spectral bands for increasing values of $R_{rs}(865)$ [Fig. 3(b)]. Nechad-type relationships (dashed lines in Fig. 3) reproduce this saturation at short visible wavelengths (443, 483 and 561 nm) and the corresponding saturated R_{rs} values (C_ρ values of the best-fitted Eq. (10)) are, respectively, 0.0185, 0.0238 and 0.0410 sr^{-1}. In the red OLI waveband, $R_{rs}(655)$ starts to reach a plateau when $R_{rs}(865)$ gets higher than 0.035 sr^{-1} and $R_{rs}(655)$ reaches the saturation value of 0.0548 sr^{-1}.
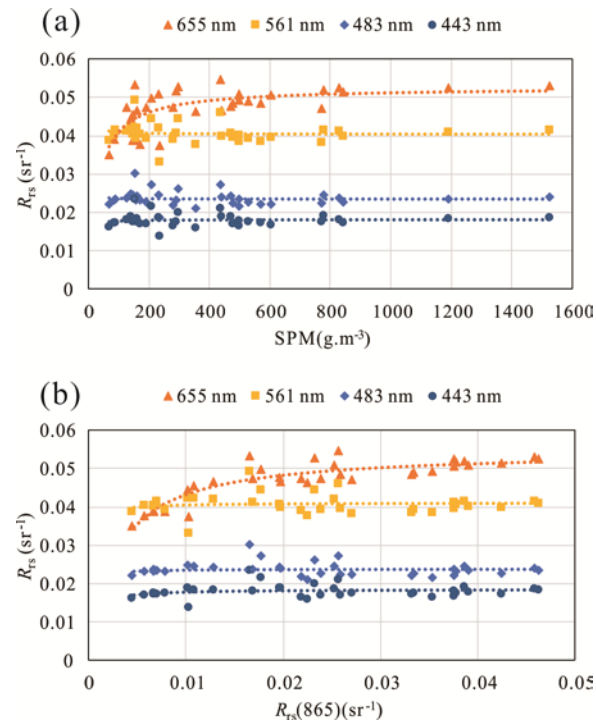

Fig. 3. R_{rs} at 443, 483, 561 and 655 nm as a function of increasing (a) SPM concentration and (b) R_{rs} at 865 nm based on field measurements carried out in the Gironde Estuary (GRE) in 2013. The dashed lines are the best-fitted Nechad-type relationships (Eq. (10)) highlighting the progressive saturation of R_{rs}.

The saturation of water reflectance is also observed, for the first time, on L8/OLI satellite data corrected for atmospheric effects (OLI images presented in Fig. 2). In the YRE [Fig. 4], R_{rs} at 443, 483, 561 and 655 nm first increases almost linearly when $R_{rs}(865)$ increases up to ~0.005 sr^{-1}. It then rapidly saturates when $R_{rs}(865)$ is higher than ~0.01 sr^{-1}. The saturation values at 443, 483 and 561 are respectively 0.0195, 0.0250 and 0.0390 sr^{-1} (C_ρ values of the best-fitted Eq. (10)). At 655 nm, the Nechad-type relationship also reproduces well the saturation of R_{rs} at 0.0588 sr^{-1}. In the SSB [Fig. 5], similar results are obtained and the corresponding R_{rs} saturation values at 443, 483, 561 and 655 nm are respectively 0.0202, 0.0256, 0.0365 and 0.0527 sr^{-1}. Lastly in the GRE [Fig. 6], the saturation of R_{rs} at 443, 483 and 561 nm occurs rapidly when $R_{rs}(865)$ is higher than 0.005 sr^{-1}. At 655 nm, R_{rs} first increases rapidly with $R_{rs}(865)$ then progressively saturates. The R_{rs} saturation values at 443, 483, 561 and 655 nm are respectively 0.0165, 0.0224, 0.0334 and 0.0477 sr^{-1}.
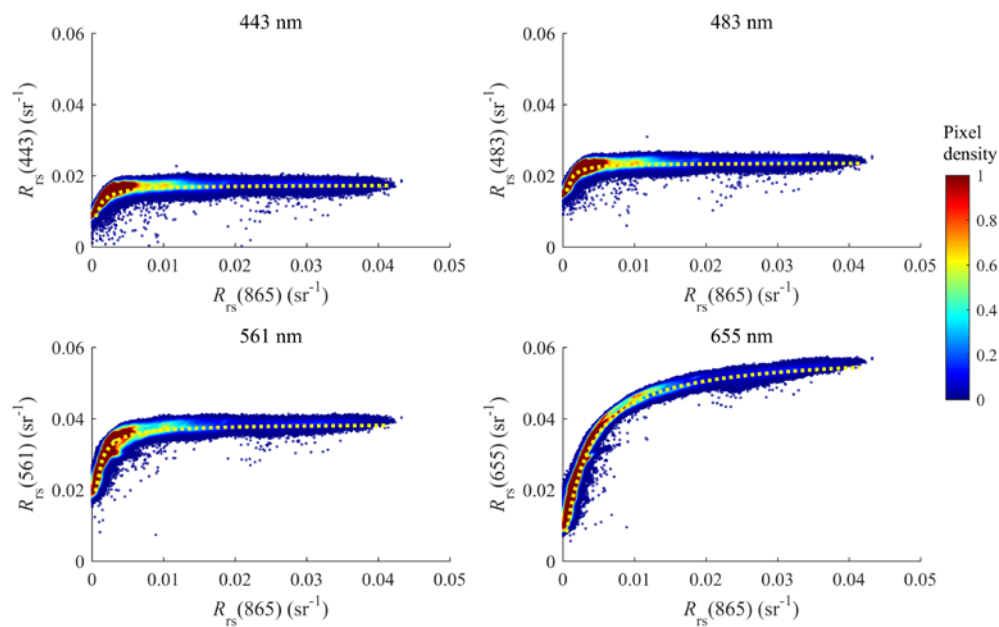

Fig. 4. L8/OLI-derived R_{rs} at 443, 483, 561 and 655 nm as a function of R_{rs} at 865 nm in the YRE (27 October 2015, image processed using the ACOLITE software applying the SWIR atmospheric correction). The yellow dashed lines represent the best-fitted Nechad-type relationships (Eq. (10)).
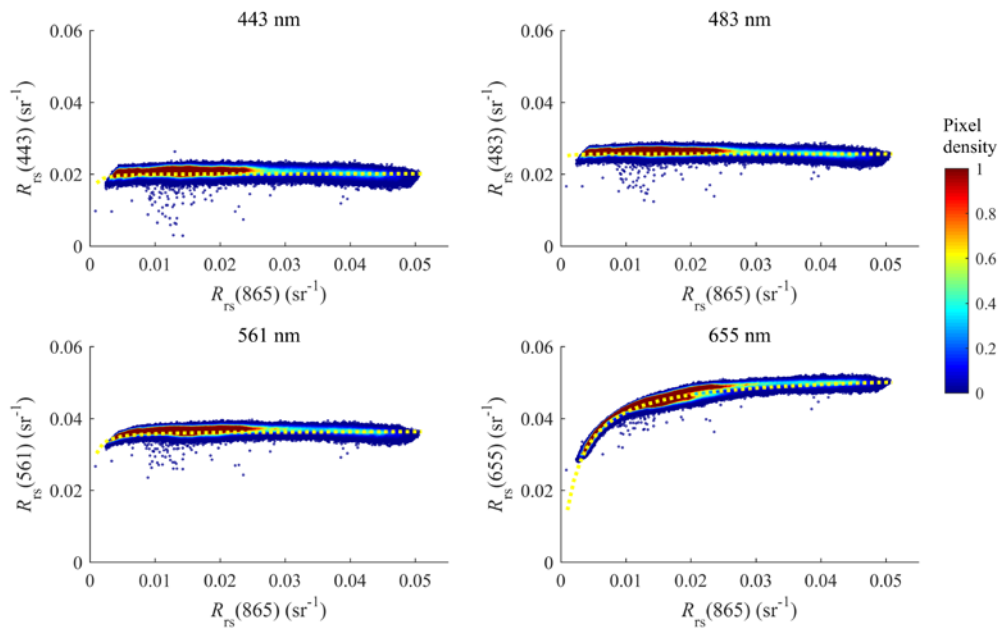
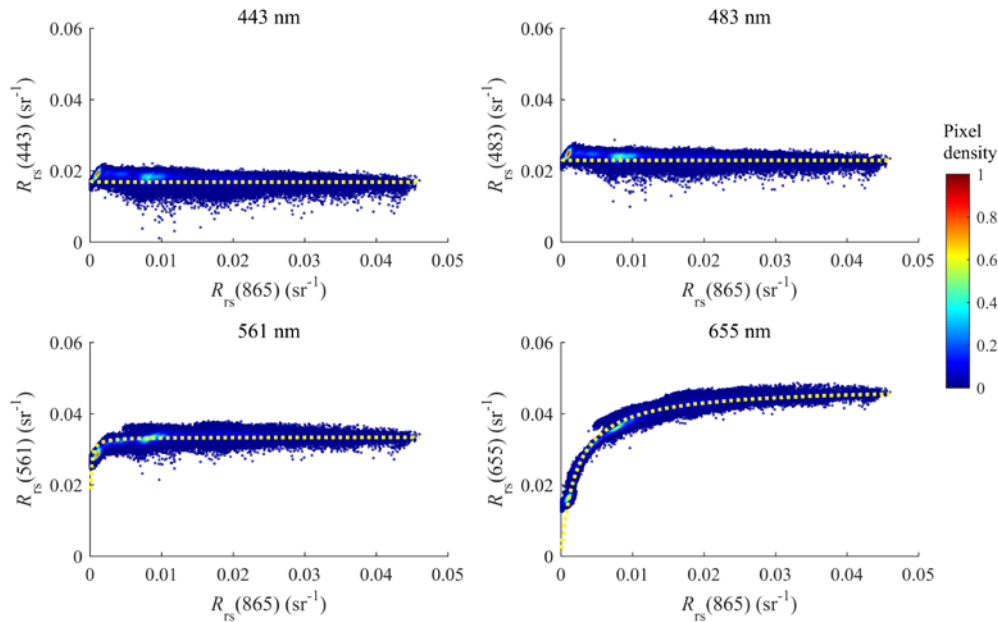Fig. 5. Same as Fig. 4 in the SSB (8 March 2017 L8/OLI image).

Fig. 6. Same as Fig. 4 in the GRE (22 February 2015 L8/OLI image).

The L8/OLI data recorded from 2013 to 2017 over the three test sites and processed using ACOLITE (SWIR atmospheric correction) can be used to highlight variations in the saturated R_{rs} values (computed as C_p values in Eq. (10)) for different tidal and seasonal conditions. In each test site, the resulting saturated R_{rs} values are quite similar [Table 2] [Fig. 7]. These quite limited variations suggest the predominance of rather similar suspended particles (in terms of

mass-specific IOPs, thus size distribution and refractive index) in the considered maximum turbidity zones. Variations are more significant from one test site to another. For example, R_{rs} saturated values in the GRE are typically 15% lower than those observed in the SSB. These variations probably reflect slightly different types of SPM (in terms of size distribution and/or composition) from one site to another. However, they are limited, probably as the three maximum turbidity zones are characterized by high concentrations of suspended sediments (mainly clays and silts with only slightly different fractions and mineral composition). In order to confirm these hypotheses, it is necessary to derive the SPM mass-specific IOPs from the observed saturated R_{rs} values.

Table 2. Saturated R_{rs} values (sr^{-1}) observed in the three test sites on different L8/OLI images. Site-by-site average values and standard deviations (SD).

| Test site	Date (yyyymmdd)	$R_{rs}(443)$	$R_{rs}(483)$	$R_{rs}(561)$	$R_{rs}(655)$
YRE	20140109	0.0197	0.0254	0.0367	0.0608
	20140125	0.0200	0.0256	0.0408	0.0632
	20150301	0.0193	0.0254	0.0394	0.0612
	20151027	0.0195	0.0250	0.0390	0.0588
	20161216	0.0231	0.0284	0.0406	0.0609
	20170306	0.0211	0.0259	0.0391	0.0595
	20170930	0.0206	0.0253	0.0401	0.0630
	Average	0.020	0.026	0.039	0.061
	SD	0.001	0.001	0.001	0.002
SSB	20131210	0.0193	0.0251	0.0366	0.0565
	20141026	0.0204	0.0249	0.0337	0.0490
	20150319	0.0202	0.0249	0.0355	0.0511
	20160218	0.0221	0.0265	0.0331	0.0497
	20160321	0.0214	0.0262	0.0369	0.0542
	20170308	0.0202	0.0256	0.0365	0.0527
	Average	0.021	0.026	0.035	0.052
	SD	0.001	0.001	0.002	0.003
GRE	20140307	0.0183	0.0239	0.0351	0.0453
	20140415	0.0122	0.0181	0.0299	0.0444
	20150222	0.0165	0.0224	0.0334	0.0477
	20170211	0.0185	0.0211	0.0296	0.0442
	20170315	0.0184	0.0243	0.0347	0.0487
	20171117	0.0157	0.0207	0.0320	0.0481
	Average	0.017	0.022	0.032	0.046
	SD	0.002	0.002	0.002	0.002
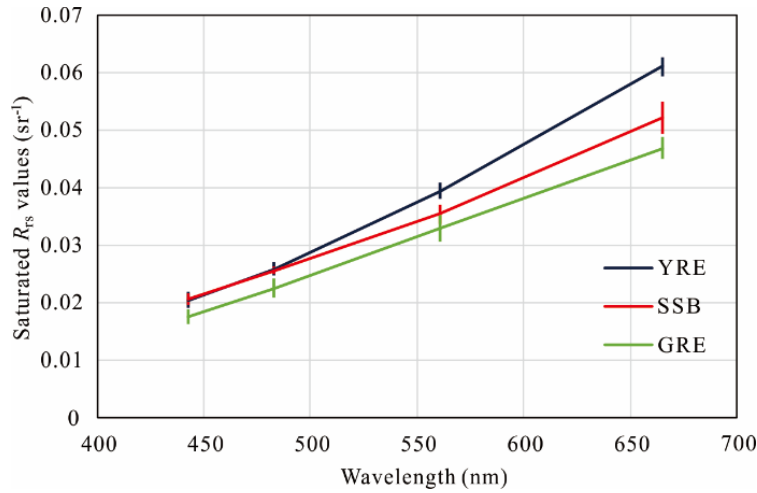
Fig. 7. Average saturated R_{rs} values (sr^{-1}) observed in the three test sites on different L8/OLI images: YRE, SSB, GRE (7, 6 and 6 images, respectively). Vertical lines show the standard deviations (SD).

3.2 Performance of semi-analytical bio-optical models in highly turbid waters

The next step was to determine the performance of the considered semi-analytical optical models in reproducing the saturation of R_{rs} in highly turbid waters. The respective performance of the Gordon models (GM_1, GM_2, GM_3), Lee et al. (2004) model (LM) and Kubelka and Munk models (KM_HQ, KM_CQ) was assessed using as reference Hydrolight outputs. For that, the Root Mean Square Error (RMSE) was computed as below:

$$RMSE = \sqrt{\frac{1}{n}\sum_{i=1}^{n}(X_i - Y_i)^2}. \qquad (11)$$

Where n is the total number of cases simulated, X_i is r_{rs} modeled using either GM, LM or KM and Y_i is the Hydrolight-computed r_{rs}.

We first compared the three different versions of the Gordon model (GM_1, GM_2 and GM_3) (not shown in Fig. 8). GM_1 and GM_2 perform well for the lowest r_{rs} values ($r_{rs} <$ 0.04 sr^{-1}), with RMSE of 0.0006 sr^{-1} and 0.0023 sr^{-1}, while GM_3 results overestimate outputs from Hydrolight when $r_{rs} <$ 0.04 sr^{-1}. When r_{rs} gets higher than ~0.06 sr^{-1}, results obtained with both GM_1 and GM_3 are slightly lower and GM_2 provides slightly higher r_{rs} values than Hydrolight. Overall, GM_1 performs better than GM_2 and GM_3 based on comparisons with Hydrolight results when $r_{rs} <$ 0.13 sr^{-1}, with RMSE of 0.0064, 0.0114 and 0.0121 sr^{-1}, respectively, so that only GM_1 (now called GM) was considered further in this intercomparison exercise together with LM, KM_HQ and KM_CQ models.

As a first approximation, an overall good agreement is observed between all the remaining semi-analytical models and Hydrolight computations. Results (r_{rs} computed using GM, LM, KM_HQ and KM_CQ plotted as a function of Hydrolight outputs) follow linear relationships close to the 1:1 line [Fig. 8]. The RMSE are respectively 0.0064, 0.0057, 0.0031 and 0.0048 sr^{-1} for the four models when $r_{rs} <$ 0.13 sr^{-1}. In more details, LM shows an overall good performance when compared to Hydrolight, especially for low (~0.01 sr^{-1}) and high (~0.13 sr^{-1}) r_{rs} values. At short wavelengths (443 and 483 nm) and for r_{rs} lower than about 0.05 sr^{-1} ($R_{rs} <$ ~0.03 sr^{-1}, $b_b/a <$ ~0.6), GM exhibits a very good performance in modeling r_{rs}, with RMSE of 0.0009 sr^{-1}, as it could be expected for a model designed for oceanic and moderately turbid waters [5,7]. However, at longer wavelengths (561, 655 and 865 nm) when r_{rs} gets higher than ~0.07 sr^{-1}, KM_HQ and KM_CQ perform better than the other models

[Fig. 8]. KM with exact Q values from Hydrolight performs well, especially when the b_b/a ratio is higher than ~0.9 (i.e., highly scattering waters where $r_{rs} > $ ~0.07 sr^{-1}, corresponding to R_{rs} values higher than ~0.04 sr^{-1}). Such high values have been measured in the field in the highly turbid waters of SSB, GRE and YRE in the yellow, red and even NIR wavelengths, but never at shorter wavelengths [7,10]. KM, designed for highly scattering media [43,44] is adapted to extremely turbid waters except at short visible and probably SWIR wavelengths where the b_b/a ratio is not high enough [7].

To summarize, based on our comparisons [Fig. 8], GM, LM and even KM_CQ (with Q a constant value of 3.6 sr) were proved to perform well enough to be considered further and model the saturation of water reflectance in highly turbid waters. KM_HQ results were also good enough, but this model needs as input Q values computed using Hydrolight. This model therefore has less *a priori* predictive ability and so was discarded at this stage.
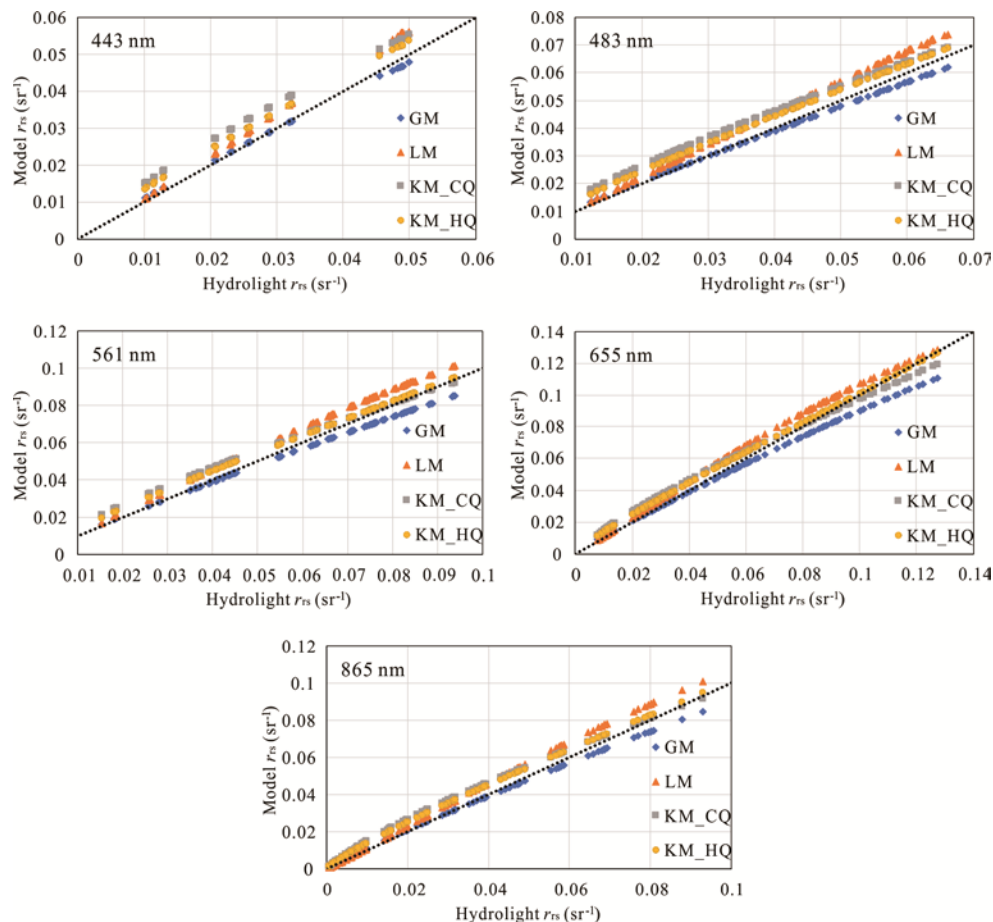

Fig. 8. Comparisons between r_{rs} values simulated at 443, 483, 561, 655 and 865 nm using different semi-analytical bio-optical models and r_{rs} values computed with Hydrolight, using the exact same IOPs as inputs. Black dots show the 1:1 lines.

3.3 Retrieval of SPM mass-specific IOPs from saturated water reflectance

Based on results presented in the previous section, three models (GM, LM and KM_CQ) are finally considered to reproduce the saturation of R_{rs} and attempt retrieval of information on the SPM mass-specific IOPs from the saturated reflectance values.

The mathematical method tested is straightforward and can be applied as soon as R_{rs} saturates at one single band (which is convenient as saturation first occurs at short visible

wavelengths). Here we assume the GM, LM and KM_CQ models to be valid in highly turbid waters and able to reproduce the observed saturation of R_{rs}, at least at the two shortest wavelengths (λ_i = 443 and 483 nm). $R_{rs}(\lambda_i)$ saturates when at a first approximation $b_b(\lambda_i) \approx b_{bp}(\lambda_i)$ and $a(\lambda_i) \approx a_p(\lambda_i)$, i.e., the a_w and b_{bw} coefficients at 443, 483 nm can be considered as negligible compared to SPM contributions, so that $b_b(\lambda_i)/(a(\lambda_i) + b_b(\lambda_i)) \approx b_{bp}*(\lambda_i)/(a_p*(\lambda_i) + b_{bp}*(\lambda_i)) = X(\lambda_i)$ and $b_b(\lambda_i)/a(\lambda_i) \approx b_{bp}*(\lambda_i)/a_p*(\lambda_i) = Y(\lambda_i)$, with $Y(\lambda_i) = X(\lambda_i)/(1-X(\lambda_i))$. In such a case, Eq. (7) (GM) can be rewritten as:

$$R_{rs}^*(\lambda_i) = C(\lambda_i) \approx 0.529 \times [0.0949 \times X(\lambda_i) + 0.0794 \times X(\lambda_i)^2] \qquad (12)$$

With $C(\lambda_i)$ a constant value, i.e., the saturated $R_{rs}(\lambda_i)$ value, and 0.529 the average value considered here for the water-air transmission factor, i.e., the air-water Fresnel reflection and refraction effects at the sea surface [46,47].

Equations (8a) and (8b) (LM) can be simplified and rewritten as:

$$G \approx 0 + G_1\left(1 - G_2 \exp\left(-G_3 \frac{b_{bp}^*(\lambda_i)}{a_p^*(\lambda_i) + b_{bp}^*(\lambda_i)}\right)\right), \qquad (13a)$$

$$R_{rs}^*(\lambda_i) = C(\lambda_i) \approx 0.529 \times 0.197 \times [1 - 0.636 \exp(-2.552 \times X(\lambda_i))] \times X(\lambda_i). \quad (13b)$$

Finally, Eq. (9) (KM_CQ) can be rewritten as:

$$R_{rs}^*(\lambda_i) = C(\lambda_i) \approx 0.529 / 3.6 \times Y(\lambda_i) / [1 + Y(\lambda_i) + (1 + 2 \times Y(\lambda_i))^{1/2}]. \qquad (14)$$

$Y(\lambda_i)$ was computed using the three models (GM, LM and KM_CQ) by inverting Eqs. (12), (13b) and (14), respectively, for the three test sites, for all the available OLI-derived R_{rs} data [Table 2] and for the GRE field data set.

Table 3. Retrieved $b_{bp}*(\lambda_i)/a_p*(\lambda_i)$ values in the three test sites using the three different models.

Test site	Model	$b_{bp}*(\lambda_i)/a_p*(\lambda_i)$					
		GM	LM	KM_CQ	GM	LM	KM_CQ
Data	λ (nm)	443	443	443	483	483	483
YRE	mean	0.47	0.40	0.38	0.64	0.51	0.52
OLI	± SD	0.04	0.03	0.03	0.04	0.03	0.03
SSB	mean	0.48	0.40	0.38	0.63	0.51	0.51
OLI	± SD	0.03	0.02	0.02	0.02	0.02	0.02
GRE	mean	0.39	0.34	0.31	0.53	0.44	0.43
OLI	± SD	0.03	0.03	0.03	0.05	0.03	0.04
GRE	in situ	0.42	0.36	0.33	0.57	0.47	0.46

Results [Table 3] highlight slightly different $b_{bp}*/a_p*$ ratio values obtained when using the three different models, in the three different test sites. These values are always slightly higher using GM than using KM_CQ and values obtained using LM are systematically in between. Values obtained in the YRE and SSB are similar, while those retrieved in the GRE (from both OLI and field data) are significantly lower. In GRE test site, the retrieved $b_{bp}*(\lambda_i)/a_p*(\lambda_i)$ ratio values obtained from OLI data are always lower than those obtained from in situ measurements. The following reasons may explain this result: first, breaking aggregates resulting in a change in their IOPs when doing the measurements. For example, Boss et al., 2009 [48] found that breakage of aggregates results in increase in beam attenuation relative to disaggregating the water, which is consistent with the difference we have obtained.

Absorption may also increase but likely less for loose aggregates. Then, the uncertainty in atmospheric correction may also result in a bias between satellite data and in situ measurements. In each test site, the $b_{bp}*/a_p*$ ratio presents moderate variations despite the various tidal and seasonal conditions covered by the OLI data and field measurements.

The retrieved $b_{bp}*(\lambda_i)/a_p*(\lambda_i)$ ratio values are quite realistic., i.e., in the expected range, taking into account the SPM mass-specific coefficients representative of turbid (sediment-dominated) coastal waters that have been reported in the literature for $b* bp(555)$ (0.0121 ± 0.0023 $m^2.g^{-1}$ [33]), $b* p(555)$ (0.5 ± 0.4 $m^2.g^{-1}$ on average [31]) and $a* p(443)$ (0.031 $m^2.g^{-1}$ [36] and 0.042 ± 0.017 $m^2.g^{-1}$ [37]). The observed variations of the $b_{bp}*/a_p*$ ratio contain valuable information concerning the regional, tidal and seasonal variations of the SPM size distribution and composition in the maximum turbidity zones that develop at the mouth of rivers. Additional work is required, however, to determine in more details the validity and limits of bio-optical models used to reproduce the saturation of R_{rs} in extremely turbid waters and uncertainties associated to the retrieved $b_{bp}*(\lambda_i)/a_p*(\lambda_i)$ ratio values. Efforts are also required to accurately measure in the field and/or in laboratory these SPM mass-specific coefficients [49,50] in order to validate the corresponding satellite products.

4. Conclusions and perspectives

The saturation of the reflectance signal in (highly) turbid waters has been observed and reported in previous studies based on field and laboratory measurements [1,9,12–16]. Our study confirms this saturation based on recent field measurements and shows, for the first time, that this water reflectance saturation is also well captured by satellite (L8/OLI) data corrected for atmospheric effects. This saturation apparently systematically occurs in the visible spectral region over the maximum turbidity zones that develop in estuarine zones such as in the three test sites considered here: the Gironde Estuary, Yellow River delta and Subei Bank. Moreover, this saturation of water reflectance can be used to retrieve information on the mass-specific absorption and backscattering coefficients of suspended particles by using adapted semi-analytical reflectance models.

Based on our field measurements, reflectance saturation occurs not only at short visible wavelengths (blue part of the spectrum) but also in the green and even red spectral regions. R_{rs} is then no longer sensitive to variations of SPM concentration but a constant value *a priori* directly related to the SPM mass-specific absorption and backscattering coefficients. L8/OLI satellite data corrected for atmospheric effects using an appropriate algorithm (here the SWIR algorithm [18]) systematically detect this water reflectance saturation in visible wavebands over the maximum turbidity zones of well-known estuarine zones. This progressive saturation of R_{rs} for increasing SPM concentration, observed from both field and satellite data, is well reproduced using the Nechad-type relationship (Eq. (10) [2],) which can be used to compute the reflectance saturation values.

The respective performance of the Gordon (GM), Lee et al. (2004) (LM) and Kubelka-Munk (KM_HQ and KM_CQ) models was assessed in the case of extremely turbid waters (SPM concentrations up to 2000 $g.m^{-3}$) using Hydrolight computations as a reference. As a first approximation, the three models tested provided rather satisfactory results and were considered further for extracting information on the SPM mass-specific IOPs from the observed saturated R_{rs} values.

Finally, using the three different models, a mathematical method was tested for the inversion of saturated water reflectance values into SPM mass-specific IOPs (backscattering to absorption coefficients ratios, $b_{bp}*/a_p*$). The results obtained proved to be quite realistic as consistent with values reported in the literature. These preliminary results are promising in the scope of remotely sensing in highly turbid waters not only the SPM concentration but also retrieving information on SPM composition and/or size distribution. Assuming the particulate IOPs in the saturated spatial domain are similar to those at areas where there is no saturation, one could also use the obtained ratio of particulate IOPs as a constraint in a reflectance

inversion to, for example, attempt to retrieve the varying CDOM concentration. This will need however further investigation, notably based on dedicated field experiments where the R_{rs} signal, SPM concentration, SPM absorption and backscattering coefficients should be measured simultaneously to test and validate optical closure.